Zika Virus Infection Prevents Host mRNA Nuclear Export by Disrupting UPF1 Function

Kristoffer Leon[1,2,3,4], Ryan Flynn[5], Mir M. Khalid[1], Krystal A. Fontaine[1], Tom Nguyen[1], G. Renuka Kumar[1], Camille R Simoneau[1,2,4], Sakshi Tomar[1], David Jimenez-Morales[1], Mariah Dunlap[1], Julia Kaye[1], Priya S Shah[1], Steven Finkbeiner[1,6,7], Nevan J Krogan[1,8,9], Carolyn Bertozzi[5,10], Jan E. Carette[11], Melanie Ott[1,2#]

[1]J. David Gladstone Institutes

[2]Department of Medicine, University of California, San Francisco

[3]Medical Scientist Training Program, University of California, San Francisco

[4]Biomedical Sciences Graduate Program, University of California, San Francisco

[5]Department of Chemistry, Stanford University, Stanford, CA

[6]Center for Systems and Therapeutics and Taube/Koret Center for Neurodegenerative Disease Research, San Francisco, CA, USA

[7]Departments of Neurology and Physiology, UCSF, San Francisco, CA, USA.

[8]Quantitative Biosciences Institute (QBI), University of California, San Francisco

[9]Department of Cellular and Molecular Pharmacology, University of California, San Francisco

[10]Howard Hughes Medical Institute, Stanford University School of Medicine, Stanford, CA

[11]Department of Microbiology and Immunology, Stanford University, Stanford, CA.

[#]Address correspondence to: melanie.ott@gladstone.ucsf.edu

Gladstone Institutes

1650 Owens Street

San Francisco, CA 9415

Abstract

Zika virus (ZIKV) is a mosquito-borne RNA virus that can infect fetuses *in utero* causing characteristic neurodevelopmental disorders including microcephaly. We previously showed that ZIKV infection downregulates expression of up-frameshift protein 1 (UPF1), a helicase/ATPase and central regulator of the nonsense-mediated mRNA decay pathway. Here, we identify a novel function of nuclear UPF1 in mRNA export. Using crosslinking immunoprecipitation of UPF1 followed by sequencing of associated transcripts as well as fluorescent in situ hybridization experiments, we find widespread mRNA accumulation in the cell nucleus of human neural progenitor cells (NPCs) upon ZIKV infection or UPF1 knockdown. Knockdown of *FREM2*, a top UPF1 target transcript encoding an extra-cellular matrix protein critical in fetal development, decreased expression of pluripotency markers and increased neuronal differentiation in NPCs, consistent with the model that trapping *FREM2* mRNA in the nucleus perturbs proper NPC function. Collectively, our data uncovers a new posttranscriptional mechanism by which ZIKV “shuts off” host mRNA export via UPF1. As we find UPF1 linked to many neurodevelopment pathways, we propose that the lack of host mRNA export contributes to virally induced neurodevelopmental disorders in ZIKV infection.

47 **Introduction**

48 Zika virus (ZIKV) is a mosquito-borne, enveloped virus with a positive sense, single
49 stranded RNA genome (Musso & Gubler, 2016). ZIKV is a member of the *Flaviviridae*
50 family that includes Dengue virus (DENV), West Nile virus (WNV) and Hepatitis C virus
51 (HCV). In 2015, an outbreak of ZIKV in Brazil was linked to a dramatic increase in the
52 number of infants born with microcephaly (Fauci & Morens, 2016; Pierson & Diamond,
53 2018). It was subsequently shown that *in utero* ZIKV infects neural progenitor cells
54 (NPCs), resulting in neurodevelopmental delays that ultimately cause a range of birth
55 defects including microcephaly, ocular damage, and contractures, collectively known as
56 congenital Zika syndrome (Costa et al., 2016; Cugola et al., 2016; Shao et al., 2016;
57 Souza et al., 2016; Tang et al., 2016). NPCs are critical for brain development because
58 they differentiate into the glial and neuronal cells that compose the majority of the brain
59 parenchyma (Martínez-Cerdeño & Noctor, 2018). Proposed molecular mechanisms by
60 which ZIKV disrupts NPC function and differentiation include perturbation of the
61 autophagy, apoptosis and unfolded protein response pathways (Ojha et al., 2018). It
62 remains unknown how ZIKV causes such widespread developmental reprogramming,
63 manipulating multiple cellular pathways at once.

64 We and others showed previously that ZIKV infection suppressed the host
65 nonsense-mediated mRNA decay (NMD) pathway (Fontaine et al., 2018; M. Li et al.,
66 2019). NMD is an RNA quality control mechanism that targets faulty host transcripts for
67 degradation and acts as an antiviral pathway on many viral species, particularly single-
68 stranded RNA viruses (Balistreri, Bognanni, & Mühlemann, 2017; Leon & Ott, 2020).
69 Different models of the NMD pathway have been described, but the exon-junction

70 complex (EJC)-mediated NMD pathway is the best defined (Kurosaki & Maquat, 2016;
71 Kurosaki, Popp, & Maquat, 2019). This pathway is classically triggered by premature
72 termination codons in mRNAs that prevent the regular displacement of EJCs from mRNAs
73 downstream of the stop codons as translation is prematurely ended (Niels H. Gehring,
74 Neu-Yilik, Schell, Hentze, & Kulozik, 2003).

75 EJCs are normally loaded onto mRNAs in the nucleus (Popp & Maquat, 2013),
76 which are exported to the cytoplasm to undergo translation, leading to proper
77 displacement of the EJCs (N. H. Gehring, Lamprinaki, Kulozik, & Hentze, 2009). Non-
78 displaced EJCs recruit the master regulator and helicase up-frameshift protein 1 (UPF1),
79 which induces a recruitment cascade activating NMD-mediated degradation of the faulty
80 transcript (Loh, Jonas, & Izaurralde, 2013; Lykke-Andersen et al., 2014). However, the
81 NMD pathway and UPF1 also target non-faulty mRNAs, especially those with long and
82 GC-rich 3' untranslated regions (UTRs), a feature found in many viral RNAs (Imamachi,
83 Salam, Suzuki, & Akimitsu, 2017; Kebaara & Atkin, 2009; Peccarelli & Kebaara, 2014;
84 Toma, Rebbapragada, Durand, & Lykke-Andersen, 2015). Because knockdown of UPF1
85 enhances replication of many RNA viruses including ZIKV, WNV, DENV, Rous Sarcoma
86 virus, Potato virus X, Pea Enation Mosaic virus 2, and Turnip Crinkle virus, NMD is
87 recognized as a *bone fide* antiviral restriction pathway, often targeted by viruses including
88 ZIKV for inactivation (Leon & Ott, 2020).

89 We previously defined how ZIKV inactivates the antiviral activity of NMD through
90 interactions between the ZIKV capsid protein and UPF1 (Fontaine et al., 2018; M. Li et
91 al., 2019). Similar interactions of capsid proteins with the NMD pathway were
92 subsequently confirmed in other flaviviruses (M. Li et al., 2019). However, ZIKV stands

93 out as infection or capsid expression selectively downregulated UPF1 expression in the
94 host nucleus (Fontaine et al., 2018). This is unusual as viral RNA replication occurs
95 exclusively in the host cytoplasm, and the role of nuclear UPF1 in ZIKV infection remains
96 unclear.

97 Here we show that UPF1 occupancy of host transcripts is globally decreased
98 during infection with many of these transcripts downregulated in the cytoplasm. ZIKV
99 infection or UPF1 knockdown resulted in polyadenylated transcript accumulation in the
100 nucleus, causing decreased protein levels of a UPF1 target and consequent perturbation
101 of NPC differentiation. We propose that by targeting nuclear UPF1 and trapping host
102 mRNAs in the nucleus, ZIKV has evolved a mechanism to “shut off” host mRNA function
103 while promoting translation of its own proteins, uncovering a new central role for UPF1 in
104 mRNA export connected to many cellular pathways associated with neurodevelopment.
105

106 **Results**

107 **ZIKV infection decreases UPF1 interaction with the 3’UTR of host transcripts**

108 While ZIKV inhibits the NMD by capsid mediated degradation of UPF1, the impact of the
109 loss of UPF1 is still unknown. We first aimed to define the UPF1-RNA binding landscape
110 by performing infrared crosslinking immunoprecipitation and RNA sequencing (irCLIP-
111 Seq) in human induced pluripotent stem cell-derived NPCs (Zarnegar et al., 2016). UPF1
112 is an RNA helicase and ATPase found associated with many transcripts (Fiorini, Bagchi,
113 Le Hir, & Croquette, 2015). To identify differences in UPF1 binding during infection, NPCs
114 were mock-infected or infected with ZIKV (isolate PRVABC59) at an MOI of 1 for 48 hours,
115 followed by UV-crosslinking of transcripts with proteins and immunoprecipitation of UPF1

116 (**Figure 1A**). RNA-protein complexes were separated by SDS-PAGE, and mass
117 spectrometry was performed on the excised bands to confirm UPF1 enrichment (**Figure**
118 **S1A, Supplemental File 1**) before RNA was extracted and submitted to next-generation
119 sequencing (**Figure 1A**, **Supplemental File 2**).

120 In mock-infected NPCs, UPF1 bound 6778 transcripts, predominantly at the
121 3'UTR, as previously reported (Kebaara & Atkin, 2009; Toma et al., 2015). In infected
122 NPCs, this number decreased to 4557 transcripts, with a marked decrease in binding at
123 the 3'UTR (**Figure 1B**). Overall, a greater than 4-fold decrease in binding was observed
124 in 3% of UPF1 target transcripts. Notably, known NMD-resistant transcripts such as
125 glyceraldehyde-3-phosphate dehydrogenase (GAPDH) maintained UPF1 interaction,
126 underscoring the central role of UPF1 in the NMD pathway (**Figure 1C**).

127 In infected samples, UPF1 also interacted with ZIKV RNA, again mostly within the
128 3'UTR, supporting the model that UPF1 targets the viral RNA to restrict infection (**Figure**
129 **1D**). To determine if viral RNA sequestered UPF1 away from host RNA (leading to
130 decreased UPF1 occupancy during infection), we quantified the percent of UPF1-bound
131 reads mapping to host vs. viral RNAs. The majority of sequences isolated with UPF1
132 pulldown mapped to the host transcriptome; viral reads only accounted for 0.33% of all
133 mapped reads, excluding a "sponge" effect of viral RNA for UPF1 **(Figure 1E).**
134

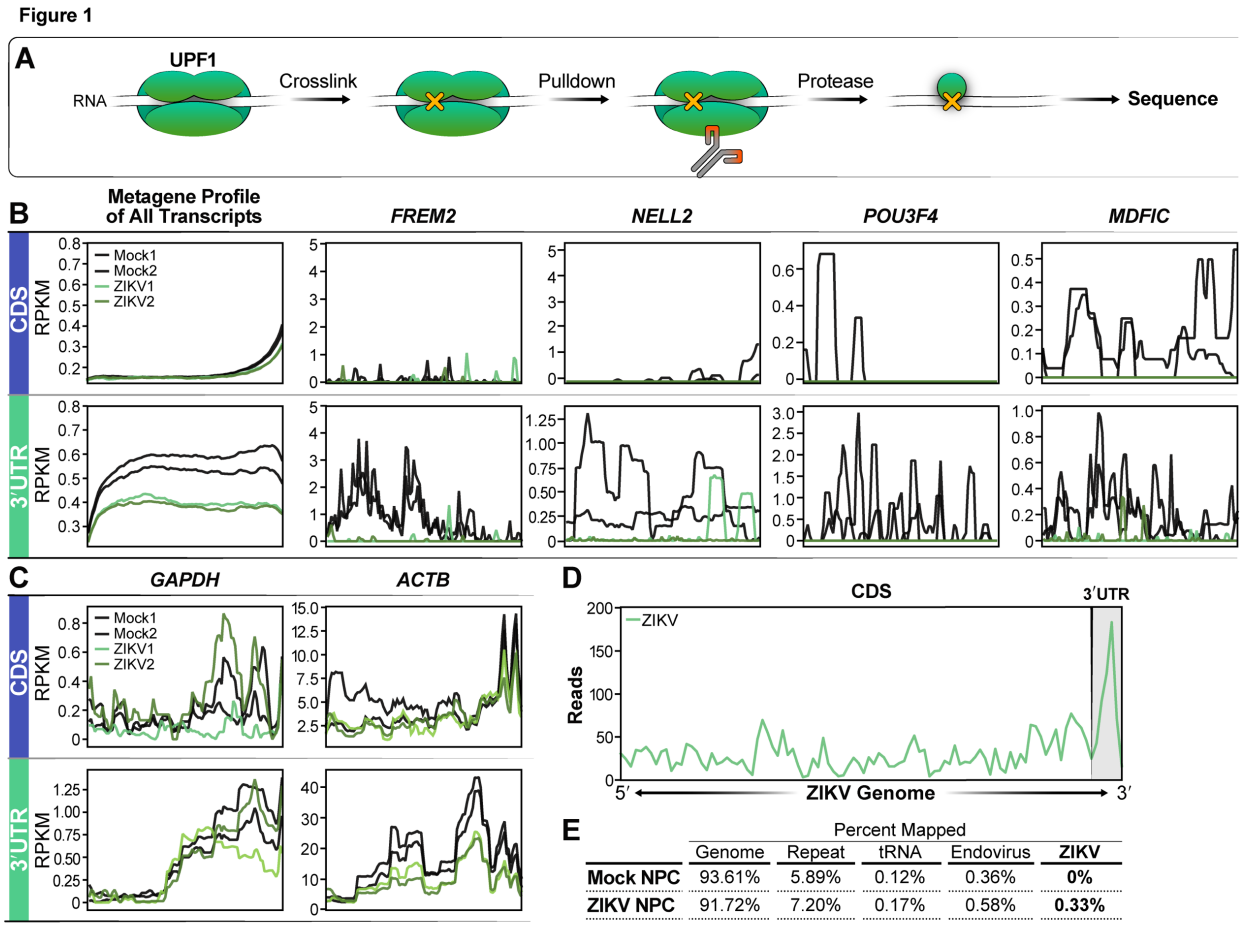

	Genome	Repeat	tRNA	Endovirus	ZIKV
Mock NPC	93.61%	5.89%	0.12%	0.36%	**0%**
ZIKV NPC	91.72%	7.20%	0.17%	0.58%	**0.33%**

Figure 1: UPF1 interactions with many host transcripts are lost during ZIKV infection of NPCs

A) irCLIP schematic describing the workflow to obtain sequencing data. After 48 hrs of ZIKV infection, UPF1 and RNA are crosslinked using UV light, followed by UPF1 pulldown and protease degradation to expose the UPF1-bound RNA for sequencing. **B)** Metagene profile of all transcripts sequenced from the irCLIP experiment. The graphs show Reads Per Kilobase of transcript, per Million mapped reads (RPKM) values for positions in the CDS and the 3'UTR. Experiment was produced from 2 biological replicates. Representative metagene plots (FREM2, NELL2, POU3F4, MDFIC) of loci found to have a loss of UPF1 interaction. **C)** A metagene plot of GAPDH, a transcript resistant to UPF1 degradation, and ACTB are shown as negative controls. **D)** Metagene plot of reads mapping to the ZIKV genome, with the 3'UTR marked. **E)** Tabular breakdown of read map percentages from the UPF1-CLIP experiment.

153 **Selective reduction of UPF1 target transcripts in the cytoplasm of infected NPCs**

154 During ZIKV infection, we saw a widespread decrease in UPF1 occupancy of host
155 transcripts. To understand the consequences of the loss of UPF1, we sought to define
156 the changes in the abundance of transcripts identified in the irCLIP-Seq experiment. We
157 performed whole transcriptome sequencing of ZIKV-infected NPCs followed by
158 differential expression analysis (**Supplemental File 3**). As expected, expression of genes
159 associated with the interferon response were predominantly upregulated upon infection,
160 consistent with previous RNA-seq studies of ZIKV-infected NPCs (C. Li et al., 2016; Liu
161 et al., 2019) (**Figure 2A, Supplemental Figure 2C**). The NMD pathway and UPF1 are
162 associated with RNA degradation, and we previously found that ZIKV infection
163 upregulated select NMD target mRNAs (Fontaine et al., 2018). We thus expected that
164 transcripts that had lost UPF1 interaction upon infection would also be selectively
165 upregulated. However, the abundance of transcripts which lost UPF1 occupancy upon
166 infection was not significantly changed, indicating that the majority of UPF1 targets were
167 not automatic subjects of NMD (**Figure 2B, Supplemental File 2**). Metascape analysis
168 of transcripts with stable abundance but a loss of UPF1 binding showed a characteristic
169 enrichment for neural and neurodevelopmental functions, underscoring the relevance of
170 UPF1 binding for proper neurodevelopment, with axon guidance being the top pathway
171 (**Figure 2C**). Axon guidance is essential for appropriate establishment of neural circuits
172 in the brain (Stoeckli, 2018).

173 Since transcript abundance was not affected by UPF1 occupancy, we next
174 hypothesized the loss of UPF1 binding may instead impact the subcellular localization of
175 cellular mRNAs. This was based on: a) UPF1 translocates between the nucleus and

176 cytoplasm, and b) we previously observed a selective downregulation of UPF1 in the cell
177 nucleus upon infection. Thus, to test this hypothesis, we fractionated ZIKV-infected NPCs
178 into cytoplasmic and nuclear compartments and performed RNA sequencing and
179 differential expression analysis with each fraction (**Supplemental File 4,5)**. We confirmed
180 successful fractionation by comparing the $\log_2$ fold change of known cytoplasmic
181 (*GAPDH*) and nuclear (*ANRIL*) transcripts, which showed 3.2-fold enrichment of *GAPDH*
182 in the cytoplasmic fraction and a 2.3-fold increase of *ANRIL* in the nuclear fraction, as
183 expected (**Supplemental Figure 2A**). We identified 585 and 312 significantly upregulated
184 mRNAs in the cytoplasm and nucleus, respectively, depicted in volcano plots showing
185 $\log_2$ fold changes of transcripts (**Figure 2D**). These upregulated transcripts were
186 predominantly interferon response genes (**Supplemental Figure 2D**). In contrast,
187 downregulated genes were overwhelmingly cytoplasmic, with 912 genes downregulated
188 in the cytoplasm compared to 22 in the nuclear fraction (**Figure 2E**). A significant overlap
189 was found between the 912 transcripts with reduced cytoplasmic expression and the 331
190 transcripts that lost UPF1 occupancy without changing overall abundance **(Figure 2F)**. In
191 contrast, considerably less overlap existed with transcripts that were upregulated in the
192 cytoplasm and had lost UPF1 binding (**Supplemental Figure 2B**). Moreover, of the top
193 53 genes with the most significant decrease in UPF1 interaction upon infection, all but 6
194 were exclusively downregulated in the cytoplasm (**Figure 2G**). These results show a
195 selective loss of UPF1 target mRNAs in the cytoplasm of infected cells. As no change in
196 total abundance was observed, we considered an accumulation of these transcripts in the
197 nucleus upon ZIKV infection.

Figure 2

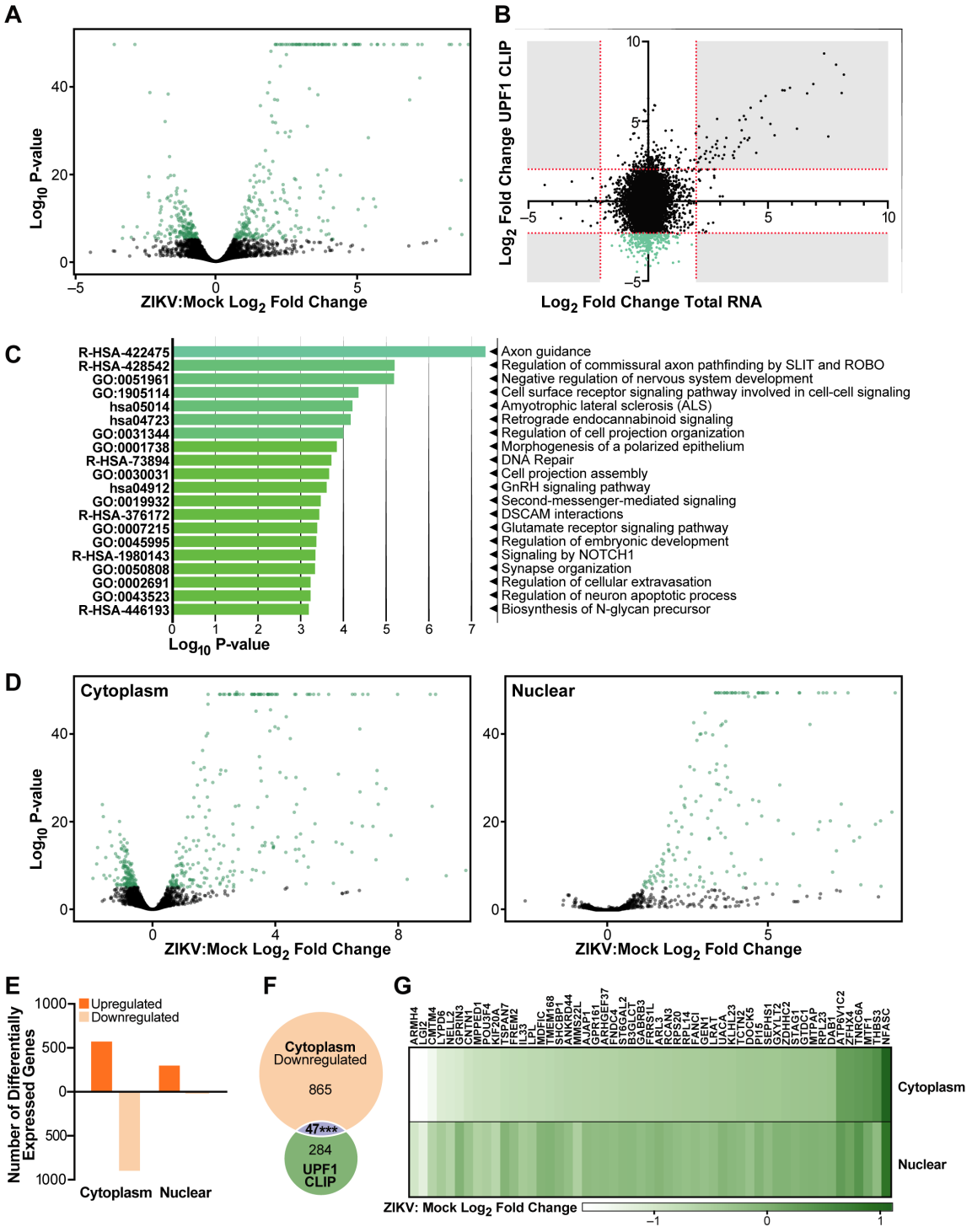

198

199

200

201 **Figure 2**: **Loss of UPF1 interaction during ZIKV infection causes mRNA**
202 **downregulation in the cytoplasm**
203 **A)** Volcano plot of whole transcriptome RNA sequencing of ZIKV infected NPCs
204 compared to Mock, n=2 biological replicates. **B)** X-axis shows ZIKV: Mock log_2 fold
205 change in whole transcriptome sequencing, Y-Axis shows ZIKV:Mock log_2 fold change
206 from the UPF1 CLIP experiment. The green transcripts are >2 log_2 fold change in the
207 UPF1-CLIP and <2 log2 fold change in total RNA. **C)** Metascape analysis of transcripts
208 identified to have a significant loss of UPF1 interaction in ZIKV infected cells compared
209 to Mock. **D)** Volcano plot of sequencing from ZIKV-infected NPCs compared to Mock
210 fractionated into cytoplasmic and nuclear fractions, n=2 biological replicates. **E)** Number
211 of differentially expressed genes from sequencing of ZIKV-infected NPCs compared to
212 Mock fractionated into cytoplasmic and nuclear fractions. **F)** Overlap of transcripts found
213 to be significantly downregulated in the cytoplasm and those with greater than a 2 log_2
214 fold decrease in the UPF1 CLIP. Statistics performed by hypergeometric probability test,
215 ***, $P \leq 0.001$. **G)** A heatmap showing log_2 fold changes of transcripts identified in the
216 CLIP experiment in cytoplasmic and nuclear fractions.
217

218 **ZIKV infection, capsid expression or UPF1 knockdown results in accumulation of**
219 **host transcripts in the nucleus**

220 To test the hypothesis that transcripts were selectively accumulating in the nucleus in
221 ZIKV-infected cells, we analyzed global transcript localization by using RNAscope
222 analysis with a polyA tail probe. We first optimized the technology in Huh7-Lunet cells, a
223 hepatoma cell line frequently used to study flavivirus infection (Vicenti et al., 2018), and
224 NPCs, both infected with ZIKV at an MOI of 1. In both cell types, polyadenylated RNA
225 fluorescence was significantly increased in the nucleus upon infection, supporting the
226 model that mRNA location rather than abundance is perturbed in ZIKV infected cells
227 (**Figure 3A,B**). To understand if this effect was UPF1-mediated, we leveraged the
228 previously demonstrated ability of ZIKV capsid to specifically degrade nuclear UPF1
229 (Fontaine et al., 2018), and used Huh7-Lunet cells expressing ZIKV capsid protein in a
230 tetracycline-inducible manner. Addition of doxycycline, and consequent expression of
231 capsid in the inducible system, lead to reduced levels of nuclear UPF1 (**Figure 3C**). This

232 also led to a similar accumulation of polyadenylated RNAs in the cell nucleus, mirroring
233 the data observed in ZIKV-infected cells (62% nuclear fluorescence in vector vs 78% in
234 capsid overexpressing cells) (**Figure 3D**). Furthermore, siRNA-mediated knockdown of
235 UPF1 in NPCs also resulted in retention of polyadenylated RNAs in the nucleus (36%
236 nuclear fluorescence in control vs 40% in siUPF1 NPCs) (**Figure 3E**) (**Supplemental**
237 **Figure 3**). Collectively, these data indicate that UPF1 regulates nuclear mRNA export, a
238 function perturbed upon nuclear UPF1 degradation during ZIKV infection.
239
240
241
242

Figure 3

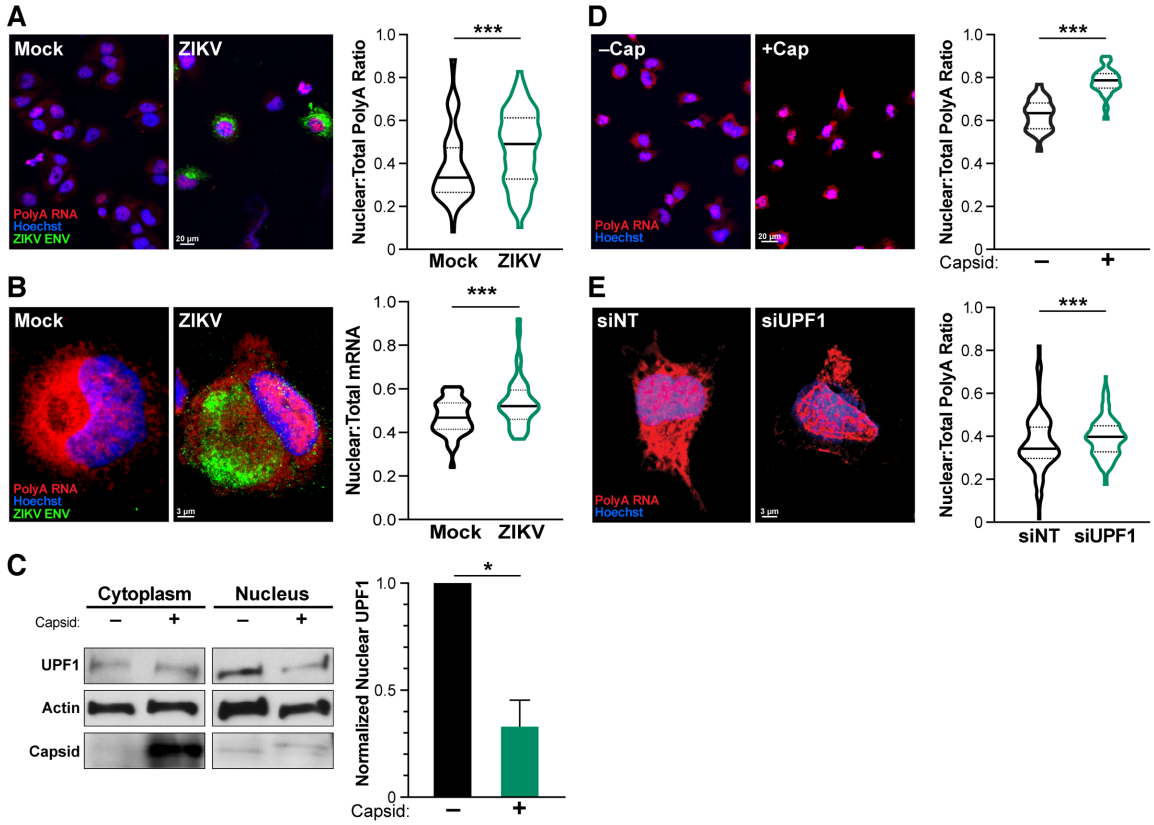

Figure 3: ZIKV-mediated degradation of UPF1 leads to mRNA retention in the nucleus.
A and B) During ZIKV infection (ZIKV ENV, green), polyA RNA (red) is shifted toward the nucleus (Hoechst, blue) in Huh7-Lunet cells. Statistics produced by a Linear Mixed Model. 3 biological replicates, n=25 cells (A) or 15 cells (B) per condition per replicate. **C)** Tetracycline-inducible Capsid expression in Huh7-Lunet cells was used to degrade nuclear UPF1. Leptomycin B (LMB) was used to increase UPF1 degradation. Statistics performed by Student's t-test, n=3, and representative western blot shown. **D)** Capsid overexpression in Huh7-Lunet cells results in an increased ratio of polyA RNAs (red) in the nucleus. N=3 biological replicates, 25 cells per condition per replicate. **E)** Knockdown of UPF1 in NPCs results in an increased ratio of polyA RNAs (red) in the nucleus. NPCs were treated with siNT and siUPF1 for 96 hours. Statistics produced by a Linear Mixed Model. n=3 biological replicates, 15 cells per condition per replicate. *, $P \leq 0.05$; **, $P \leq 0.01$; ***, $P \leq 0.001$. Error bars are SEM.

261 **FREM2, a UPF1 target, regulates NPC differentiation**

262 Next, we focused on *FREM2*, the transcript with the largest fold decrease in UPF1
263 interaction in the irCLIP studies (**Figure 1B**). FREM2 is an extracellular matrix protein
264 involved in cell-cell interactions that is important in many developmental pathways
265 including tissue and vascular morphogenesis (Pavlakis, Chiotaki, & Chalepakis, 2011;
266 Timmer, Mak, Manova, Anderson, & Niswander, 2005). The *FREM2* transcript was also
267 specifically downregulated in the cytoplasm of infected NPCs (**Figure 2G**). We confirmed
268 select cytoplasmic downregulation of *FREM2* mRNA expression upon infection by qPCR
269 (**Figure 4A**). Using RNAscope, we found enrichment of the *FREM2* transcript in the
270 nucleus of cells treated with UPF1-targeting siRNAs as compared to cells treated with
271 non-targeting control siRNAs, where it was found in both the cytoplasm and the nucleus
272 (**Figure 4B**). FREM2 protein levels were significantly decreased in UPF1 siRNA-treated
273 cells (42% decrease in siUPF1 compared to the siNT control), supporting the model that
274 nuclear mRNA retention leads to reduced translation of UPF1 target transcripts upon
275 ZIKV infection (**Figure 4C**).

276 To determine the functional consequences of reduced FREM2 expression, we
277 used siRNAs to knockdown FREM2 in NPCs (**Supplemental Figure 4).** FREM2
278 knockdown increased the percentage of cells expressing βIII-Tubulin (neuronal marker)
279 by 44%, and decreased the percentage of cells expressing Sox2 (pluripotency marker)
280 by 51% (**Figure 4D**). This indicates that by preventing FREM2 nuclear export and protein
281 expression, ZIKV infection may promote premature neuronal differentiation of NPCs, thus
282 reducing the number of NPCs that determine brain and ultimately head size.

283

Figure 4

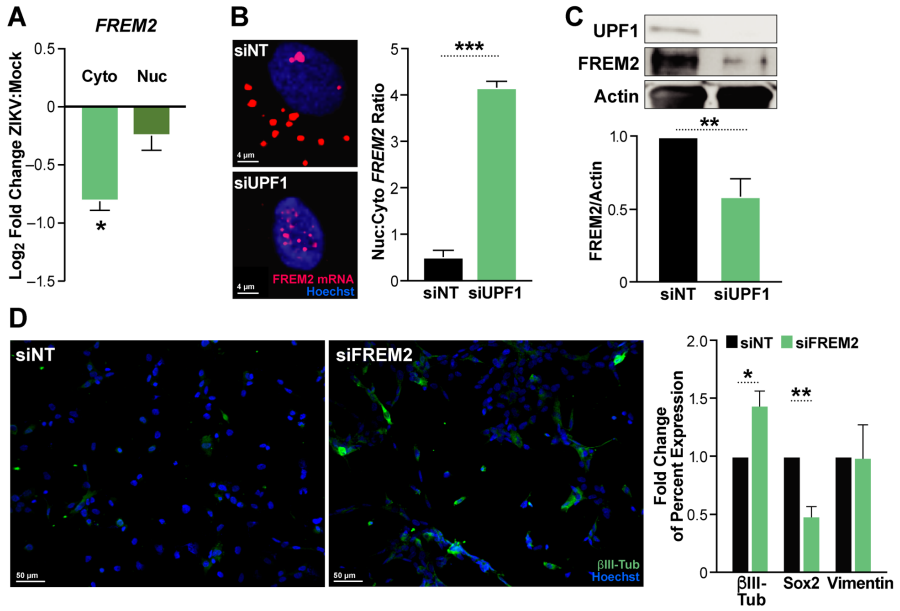

Figure 4: UPF1 knockdown leads to retention of *FREM2* mRNA and decreased protein production, which causes premature differentiation of NPCs.
A) qPCR of *FREM2* in cytoplasmic and nuclear fractions in ZIKV infected NPCs. **B)** RNAscope of *FREM2* in UPF1 knockdown NPCs. NPCs were treated with siRNAs for 96 hours prior to harvesting for microscopy. Number of nuclear puncta compared to cytoplasmic as calculated by Imaris. 3 biological replicates, 10 cells per biological replicate per condition averaged. Statistics produced by Student's t-test. **C)** Western blot of siNT and siUPF1 treated NPCs. NPCs were treated with siRNAs for 96 hours prior to harvesting for microscopy. Densitometric analyses of FREM2 were performed using ImageJ to quantify relative band intensities. **D)** siNT and siFREM2 treated NPCs stained for βIII-Tubulin, Soxs2 and Vimentin. NPCs were treated with siRNAs for 7 days prior to analysis. Statistics produced by Student's t-test. *, $P \leq 0.05$; **, $P \leq 0.01$; ***, $P \leq 0.001$. Error bars are SEM.

304 **Discussion**

305 In this study, we identified a novel mechanism by which ZIKV infection prevents RNA
306 export from the nucleus, a phenotype described in other viral infections, but not seen
307 previously with flaviviruses (Fortes, Beloso, & Ortín, 1994; Kumar & Glaunsinger, 2010;
308 Kuss, Mata, Zhang, & Fontoura, 2013; Sakuma et al., 2014). We determine that many
309 transcripts lost UPF1 occupancy during ZIKV infection, especially in the 3'UTR, consistent
310 with the finding that UPF1 expression is downregulated in ZIKV infection. Loss of UPF1
311 binding altered transcript localization with only a minor effect on transcript abundance,
312 underscoring the functional significance of UPF1's role in mRNA export. The
313 accumulation of mRNA in the nucleus induced by ZIKV infection could be recapitulated
314 both by ZIKV capsid expression known to degrade nuclear UPF1 and by UPF1
315 knockdown, linking UPF1's new function with its nuclear localization. Lastly, we show that
316 when UPF1 is unable to export *FREM2* mRNA from the nucleus, FREM2 protein
317 abundance decreases, ultimately disrupting neural differentiation. The majority of these
318 experiments were performed in human NPCs, the natural target cells of ZIKV in fetuses,
319 providing a physiologically relevant view into pathways and transcripts disrupted by ZIKV
320 infection and how that might lead to congenital Zika syndrome.

321 UPF1 is an RNA helicase involved with a plethora of functions within the cell.
322 Besides its function in NMD, it also plays important roles in several other RNA decay
323 pathways (Kim & Maquat, 2019), as well as telomere maintenance (Chawla et al., 2011),
324 and ubiquitination (Feng, Jagannathan, & Bradley, 2017). While this study was underway,
325 a study in fruit flies connected nuclear UPF1 function with co-transcriptional binding and

326 export of mRNAs from the nucleus (Singh et al., 2019). UPF1 is also required for HIV
327 RNA export from the nucleus (Ajamian et al., 2015).

328 Here we show a role of nuclear UPF1 in mRNA export in mammalian cells, a role
329 prominently targeted by ZIKV. While the precise mechanisms of UPF1 mediated nuclear
330 export are not yet clear, two findings underscore its significance: 1) most transcripts are
331 not upregulated in NPCs after loss of UPF1 binding, which points to another major
332 function of UPF1 in cells besides NMD, and 2) many polyadenylated transcripts are
333 retained in the nucleus upon UPF1 knockdown, demonstrating that the effect of UPF1 on
334 mRNA export is widespread. Additional studies are needed to determine whether specific
335 features of these mRNAs, such as the 3'UTR sequence or structure, underlie their
336 targeting for export by UPF1 (Carmody & Wente, 2009). This includes UPF1 binding to
337 ZIKV RNA and the features that lead to UPF1 enrichment in the viral 3'UTR. Interestingly,
338 a non-coding subgenomic flavivirus RNA (SfRNA) is derived from the 3' UTR of ZIKV and
339 is known to be resistant to XRN1 degradation (Göertz, Abbo, Fros, & Pijlman, 2018). The
340 production of an SfRNA is shared among flaviviruses and antagonizes the interferon
341 response. UPF1 interaction with the SfRNA is potentially important for ZIKV replication
342 and would be important to explore in future studies.

343 The host shutoff effect is a common viral strategy to reduce host gene expression,
344 potentially for the purposes of competing with cellular resources and evading immune
345 responses. Flaviviruses have been reported to cause host shutoff by translational
346 repression (Roth et al., 2017). The host shutoff described here is achieved by retention
347 of host transcripts in the nucleus. We confirm that a single viral protein, the capsid protein,
348 is sufficient to specifically degrade nuclear UPF1 and cause nuclear mRNA retention.

349 This underscores the importance of the localization of ZIKV capsid to the cell nucleus
350 (Oliveira, Mohana-Borges, de Alencastro, & Horta, 2017), which is independent from its
351 function as a structural component of the virion as the virus replicates exclusively outside
352 of the nucleus (Mohd Ropidi, Khazali, Nor Rashid, & Yusof, 2020). This also highlights
353 the significance of nuclear UPF1, which is less studied as compared to cytoplasmic UPF1.
354 UPF1 has been associated with a number of roles in the nucleus, including cell cycle
355 progression, DNA replication, telomere maintenance, and mRNA release (Singh et al.,
356 2019; Varsally & Brogna, 2012).

357 The nuclear retention of host mRNAs caused by the disruption of UPF1 function
358 could contribute to the neurodevelopmental defects seen during fetal ZIKV infections. As
359 it impacts many mRNAs, it may represent a central mechanism explaining pleotropic
360 effects of ZIKV infection on many cellular pathways. Here we follow up on *FREM2* as a
361 top UPF1 target and show that it is downregulated at the protein level when UPF1 is
362 unable to perform its role as a nuclear mRNA export regulator. FREM2 is both a member
363 of the FRAS/FREM complex and regulates its formation (Pavlakis et al., 2011). The
364 FRAS/FREM complex is found in cellular basement membranes and is expressed
365 differentially during development (Timmer et al., 2005). FREM2 itself is important for
366 proper development of the eye and mutation is associated with Fraser syndrome, in which
367 cryptopthalamos (a congenital defect where the eyes are covered completely by skin and
368 often associated with small or missing eyeballs) is commonly seen (Slavotinek & Tifft,
369 2002). As developmental defects in the eyes are also seen in children with congenital
370 Zika syndrome, the retention of the *FREM2* transcript in the nucleus could be directly

371 involved in pathogenesis (de Paula Freitas, Ventura, Maia, & Belfort, 2017; Ventura &
372 Ventura, 2018).

373 Our studies in NPCs and Huh7 hepatoma cells show that at least in these cell
374 types UPF1's role in nuclear export affects more mRNAs than its known function in NMD.
375 How this function is regulated and whether it involves known UPF1 interacting proteins
376 such as the EJC or the known RNA export pathways such as CRM-1, remains to be
377 determined. The finding that ZIKV has evolved a mechanism to selectively target nuclear
378 UPF1 and the mRNA export function of the protein underscores its central yet so far
379 underappreciated role in biology.

380

381 **Materials and Methods**

382 *Cell Culture and Viruses*

383 Human iPSC-derived NPCs were generated and maintained as described previously
384 (Consortium, 2017). The human fibroblast cell line used to generate iPSCs came from
385 the Coriell Institute for Medical Research and Yale Stem Cell Center. The iPSCs used in
386 these studies was the CTRL2493n17 line. CTRL2493n17 was derived from the parental
387 fibroblast line ND31845 that was biopsied from a healthy female at 71 years of age. iPSCs
388 were cultured and maintained in complete mTESR (StemCell Techologies). NPCs were
389 differentiated and maintained using EFH media (Stemline Neural Stem Cell Media [Sigma
390 Aldrich], EGF [R&D Biosystems], rhFGF basic [R&D Biosystems]. Heparin Sulfate [Sigma
391 Aldrich]). NPCs were dissociated and plated onto Matrigel-coated plates (Corning) prior
392 to infecting with ZIKV (MOI of 1) or treating with siRNAs. Experiments were harvested 48
393 hours post infection and up to 7 days after siRNA treatment. Huh7-Lunet cells (Ralf

394 Bartenschlager, Heidelberg University), and Vero cells were maintained in Dulbecco's
395 modified Eagle's medium (DMEM) with 10% fetal bovine serum (FBS), 2 mM l-glutamine,
396 100 U/ml penicillin, and 100 µg/ml streptomycin.
397
398 N-terminally Strep TagII tagged ZIKV Capsid was cloned to pLVX-TetOne-Puro Vector
399 (Clontech, Cat: 631849) using BamHI & EcoRI cut sites. We used a 2nd generation
400 lentiviral system to generate a stably expressing ZIKV Capsid Huh7-Lunet cell line. After
401 transduction Huh7-Lunet cells were selected with puromycin (2ug/ml) for one weeks and
402 later clonally expanded. Clones with the highest & specific expression was used for
403 experiment. Huh7-Lunets were maintained in DMEM with 10% FBS, P/S and L-glut.
404
405 The strain PRVABC59 of ZIKV (ATCC VR-1843) was used for all experiments. ZIKV
406 stocks were propagated in Vero cells (ATCC), and titers were determined by plaque
407 assays on Vero cells. ZIKV infections were performed by adding viral inoculum to DMEM
408 with 2% FBS or EFH followed by a two-hour incubation at 37C with a rock every 15
409 minutes. After infection was completed, inoculum was aspirated and then fresh DMEM
410 with 10% FBS or EFH was added to the cells. Infected cells were cultured for 48 hours
411 prior to harvesting for all sequencing and IF experiments.
412
413 *Antibodies and other reagents*
414 Primary antibodies used were anti-UPF1 (Bethyl laboratories, A300-38A, CST, 12040S
415 and Abcam, ab109363), anti-FREM2 (Invitrogen, PA5-20982), anti-FLAG (Abcam,
416 ab18230), anti-Actin (CST, 4967S), anti-GFAP (Abcam, ab53554), anti-Nestin (Abcam,

417 ab22035) and anti-Beta III tubulin (Abcam, ab18207). Secondary antibodies used include
418 goat anti-rabbit Alexa 488 (Invitrogen, A-11008), goat anti-mouse Alexa 488 (Invitrogen,
419 A-11001), goat anti-rabbit Alexa 594 (Invitrogen, A-11012), goat anti-mouse Alexa 594
420 (Invitrogen, A-11005), donkey anti-goat Alexa 647 (Invitrogen, A-21447), donkey anti-
421 rabbit Alexa 488 (Invitrogen, A-21206), donkey anti-mouse Alexa 594 (Invitrogen, A-
422 21203). The RNAScope Multiplex Fluorescent V2 Assay (ACD, 323100) was used with
423 RNAscope Probes include polyA RNA (ACD, 318631) and FREM2 (ACD, 482841).
424 Opal570 (Akoya Biosciences, FP1488001KT) were used for visualization of RNAscope
425 probes. Accell siRNA was used for knockdown of FREM2 (Dharmacon, E-021693-00-
426 0010) and UPF1 (Dharmacon, E-011763-00-0010) according to manufacturer's
427 instructions. Non-targeting siRNAs used were cat. D-001910-10-20 (Dharmacon). Huh7-
428 Lunets were treated with 60 ng/mL of Leptomycin B (Cayman Chemical) for 16 hours.
429
430 *Infrared Crosslinking and Immunoprecipitation*
431 irCLIP was performed as in Zarnegar et al. 2016 (BJ et al., 2016). HeLa cells grown as
432 described above and UV crosslinked to a total of 0.35 J/cm^2. Whole-cell lysates were
433 generated in CLIP lysis buffer (50 mM HEPES, 200 mM NaCl, 1 mM EDTA, 10% glycerol,
434 0.1% NP-40, 0.2% Triton X-100, 0.5% N-lauroylsarcosine) and briefly sonicated using a
435 probe-tip Branson sonicator to solubilize chromatin. Each experiment was normalized for
436 total protein amount, typically 1 mg, and partially digested with RNase A (ThermoFisher
437 Scientific, EN0531) for 10 minutes at 37°C and quenched on ice. UPF1 (Bethyl
438 laboratories, A300-38A) IP's were performed, 15 μg each antibody with 50 μL Protein G
439 Dynabeads (ThermoFisher Scientific), for 8 hours at 4°C on rotation. Samples were

440 washed sequentially in 1 mL for 1 minutes each at 25°C: 1× high stringency buffer (15 mM
441 Tris-HCl, pH 7.5, 5 mM EDTA, 2.5 mM EGTA, 1% Triton X-100, 1% sodium
442 deoxycholate, 120 mM NaCl, 25 mM KCl), 1× high salt buffer (15 mM Tris-HCl pH 7.5,
443 5 mM EDTA, 2.5 mM EGTA, 1% Triton X-100, 1% sodium deoxycholate, 1 M NaCl), 2×
444 NT2 buffer (50 mM Tris-HCl, pH 7.5, 150 mM NaCl, 1 mM $MgCl_2$, 0.05% NP-40). After
445 the NT2 wash, RNA-protein complexes were dephosphorylated with T4 PNK (NEB) for
446 45 minutes in an Eppendorf Thermomixer at 37°C, 15 seconds 1400rpm, 90 seconds of
447 rest in a 30 μL reaction, pH 6.5, containing 10 units of T4 PNK, 0.1 μL SUPERase-IN
448 (ThermoFisher Scientific), and 6 μL of PEG-400 (16.7% final). Dephosphorylated RNA-
449 protein complexes were then rinsed once with NT2 buffer and 3'-end ligated with T4 RNA
450 Ligase 1 (NEB) overnight in an Eppendorf Thermomixer at 16°C, 15 seconds 1400rpm,
451 90 seconds of rest in a 60 μL reaction containing 10 units T4 RNA Ligase, 1.5 pmol pre-
452 adenylated-IR800-3'biotin DNA-adapter, 0.1 μL SUPERase-IN, and 6 μL of PEG400
453 (16.7% final). The following day, samples were again rinsed once with 500 μL NT2 buffer
454 and resuspended in 30μL of 20 mM DTT, 1x LDS (ThermoFisher Scientific) in NT2 buffer.
455 Samples were headed to 75°C for 10 min, and released RNA-protein complexes were
456 separated on 4-12% Bis-Tris SDS-PAGE (1.0mm X 12 well) at 200V for 45 min. Resolved
457 RNP complexes were wet-transferred to nitrocellulose at 550 mA for 45 minutes at 4°C.
458
459 Nitrocellulose membranes were imaged using an Odyssey CLx scanner (LiCor), RBP-
460 RNA complexes were excised using scalpels, and RNA was recovered by adding 0.1 mL
461 of Proteinase K reaction buffer (100 mM Tris, pH 7.5, 50 mM NaCl, 1 mM EDTA, 0.2%
462 SDS) and 5 μL of 20mg/mL Proteinase K (ThermoFisher Scientific). Proteins were

463 digested for 60 minutes at 50°C in an Eppendorf Thermomixer. Next, 200 μL of saturated-
464 phenol-chloroform, pH, 6.7 was added to each tube and incubated for 10 minutes at 37°C
465 in an Eppendorf Thermomixer, 1400 rpm. Tubes were briefly centrifuged and the entire
466 contents transferred to a 2 mL Heavy Phase Lock Gel (5Prime, 2302830). Samples were
467 centrifuged for 2 minutes at >13000 rpm. The aqueous layer was re-extracted with 1 mL
468 of chloroform (inverting 10 times to mix; no vortexing) in the same 2 mL Phase Lock Gel
469 tube and centrifuged for 2 minutes at >13000 rpm. The aqueous layer was then
470 transferred to a new 2 mL Heavy Phase Lock Gel tube and extracted again with an
471 additional 1 mL of chloroform. After 2 minutes centrifugation at >13000 rpm, the aqueous
472 layer was transferred to a siliconized 1.5 mL tube and precipitated overnight at -20°C by
473 addition of 10 μL 5M NaCl, 3 μL Linear Polyacrylamide (ThermoFisher Scientific) and 0.8
474 mL 100% ethanol. RNA fragments were pelleted at >13000 rpm for 45 minutes at 4°C,
475 washed once with 1 mL of ice cold 75% ethanol and air dried.
476
477 RNA pellets were resuspended in 12 μL water 1 μL of 3 μM cDNA and 1 μL of 10mM
478 dNTPs and heated to 70°C for 5 minutes then rapidly cooled to 4°C. cDNA Master Mix (4
479 μL 5x Super Script IV (SSIV) Buffer, 1 μL 100mM DTT, 1 μL SSIV, 6 μL total) was added
480 to the annealed RNA and incubated for 30minutes at 55°C. cDNA:RNA hybrids were
481 captured by addition of 5 μL of MyOne Streptavidin C1 Dynabeads (ThermoFisher
482 Scientific) that had been rinsed and suspended in 50 μL of Biotin-IP buffer (100mM Tris,
483 pH 7.5, 1M NaCl, 1mM EDTA, 0.1% Tween), and end over end rotation for 45 minutes at
484 room temperature. Beads were placed on a 96-well magnet and washed sequentially
485 twice with 100 μL of Biotin IP buffer and 100 μL ice-cold 1xPBS. Beads were resuspended

486 in 10 μL of cDNA elution buffer (8.25 μL water, 1 μL of 1 μM P3 short oligo, and 0.75 μl
487 of 50 mM $MnCl_2$) and headed to 95°C for 10 minutes, ramp 0.1 degree/second to 60°C
488 forever. Next 5 μL of circularization reaction buffer (3.3 μL water, 1.5 μL 10x Circligase-II
489 buffer, and 0.5 μL of Circligase-II (Epicentre)). cDNA was circularized for 2 hours at 60°C.
490 cDNA was purified with 30 μL of AMPure XP beads (Beckman Coulter) and 75 μL of
491 isopropanol. Samples were incubated for 20 minutes at 25°C, washed twice with 100 μL
492 80% ethanol, air dried for 5 minutes, and eluted in 14 μL of water. Elution took place at
493 95°C for 3 minutes and immediately transferred to a 96-well magnet. Eluted cDNA was
494 transferred to a new PCR tube containing 15 μL of 2X Phusion HF-PCR Master Mix
495 (NEB), 0.5 μL of 30 μM P3/P6 PCR1 oligo mix and 0.5 μl of 15x SYBR Green I
496 (ThermoFisher Scientific). Real-time quantitative PCR was preformed: 98°C 2 min, 15
497 cycles of 98°C 15 seconds, 65°C 30 seconds, 72°C, 30 seconds, with data acquisition
498 set to the 72°C extension. PCR1 reactions were cleaned up by adding of 4.5 μL of
499 isopropanol, 54 μL of AMPure XP beads and incubation for 10 min. Beads were washed
500 once with 80% ethanol, dried for 5 min, and eluted in 15 μl of water. Illumina flow cell
501 adaptors were added by adding 15 μL 2X Phusion HF-PCR Master Mix and 0.4 μL
502 P3solexa/P6solexa oligo mix and amplified: 98°C 2 min, 3 cycles of 98°C 15 seconds,
503 65°C 30 seconds, 72°C, 30s seconds. Final libraries were purified by addition of 48 μL of
504 AMPure XP beads and incubation for 5 min. Beads were washed twice with 70% ethanol,
505 dried for 5 min, and eluted in 20 μL of water. 1-2μL of libraries were quantitated by HS-
506 DNA Bioanalyzer. Samples were deep sequenced on the Illumina NextSeq machine:
507 single-end, no index, high-output, 75-bp cycle run.
508

509 Whole transcriptome RNA sequencing was performed using the same above method for
510 RNA extraction, library preparation and sequencing.
511
512 *Nuclear/cytoplasmic RNA fractionation and sequencing*
513 Fractionation was performed using the Cytoplasmic and Nuclear RNA Purification Kit
514 (Cat. # 2100, Norgen Biotek Corp). Purified RNA was treated with DNase I followed by
515 library preparation using the NuGEN V2 RNA-Sequencing Library Preparation kit (Tecan
516 Genomics). Both RNA and library quality were analyzed via a Bioanalyzer (Agilent).
517 Sequencing was performed on a NextSeq 500 (Illumina): single-end, no index, high-
518 output, 75-bp cycle run.
519
520 *IF and RNAscope protocol*
521 For immunofluorescence and RNAscope, infected NPCs were collected at 48 hr and
522 plated onto 22- by 22-mm no. 1.5 coverslips. Cells were then fixed with 4% PFA in PBS
523 for 15 minutes. For the RNAscope protocol, we followed manufacturer's instructions for
524 adherent cell lines. Briefly, we first dehydrated the cells using 50%, 70% and then 100%
525 ethanol in PBS. This was followed by a rehydration of the cells using 70% and then 50%
526 of ethanol in PBS. Lastly, cells were fully rehydrated in PBS. Cells were then
527 permeabilized by hydrogen peroxide, followed by protease 3 treatment. Next, we
528 hybridized the RNAscope probes to the cells for 2 hours or O/N at 40C. Probe
529 amplification was then performed, followed by labelling with Opal570 (Akoya
530 Biosciences). Nuclei were stained using Hoechst 33258 (Thermofisher).
531

532 For immunofluorescence, cells were fixed, permeabilized by 0.1% Triton X-100 (Sigma
533 Aldrich), blocked with 3% bovine serum albumin (Sigma Aldrich) in PBS. Cells were then
534 immunostained with the indicated antibody, followed by the appropriate secondary.
535 Lastly, nuclei were stained with Hoechst 33258.
536
537 Microscopy was performed on an LSM880 with Airyscan (Zeiss) or an Olympus
538 FV3000RS. On the LSM880, imaging of Huh7-Lunet cells were performed with 20x
539 magnification objective, while NPCs were imaged with a 63x oil objective. On the
540 FV3000RS, the 20x objective was used for imaging NPCs. All images were taken as a Z-
541 stack.
542
543 *Western blot analysis*
544 Cells were lysed in RIPA lysis buffer (50 mM Tris-HCl [pH 8], 150 mM NaCl, 1% NP-40,
545 0.5% sodium deoxycholate, 0.1% SDS, supplemented with Halt protease inhibitor cocktail
546 [Thermo Fisher Scientific]) to obtain whole-cell lysates or lysed using the NE-PER nuclear
547 and cytoplasmic extraction kit (Thermo Fisher Scientific) to obtain cytoplasmic and
548 nuclear fractions. Proteins were separated by SDS-PAGE and transferred to
549 nitrocellulose membranes (Bio-Rad). Proteins were visualized by chemiluminescent
550 detection with ECL and visualized on a ChemiDoc MP Imaging System (Bio-Rad).
551
552 *Computational and Statistical Analyses*
553 For western blot analysis, differences in band intensity were quantified by densitometry
554 using ImageJ (Schneider, Rasband, & Eliceiri, 2012). Student's t-test was used for

555 statistical analysis of Western Blots. Imaris (Oxford Instruments) was used for analysis of
556 confocal images, using the surface function for polyA mRNA analysis and dot function
557 identifying specific transcripts by RNA-scope. Nuclei were also bounded and identified by
558 the surface function of Imaris. PolyA RNA-scope experiments were statistically analyzed
559 using a linear mixed model to account for individual cell values across multiple biological
560 replicates. Data are represented as means plus standard errors of the means (SEM).
561 Gene set overlap statistics were performed using a hypergeometric test. Statistical
562 significance was defined as follows: *, $P \leq 0.05$; **, $P \leq 0.01$; ***, $P \leq 0.001$; ****, P
563 ≤ 0.0001. Biological replicates are defined as the same experimental design but
564 performed sequentially, with a different cell passage number and on different days.
565
566 *Analysis of RNA sequencing data*
567 PCR duplicates were removed using unique molecular identifiers in the RT primer region.
568 The adaptor and barcode sequences were trimmed and reads were mapped step-wise to
569 viral (ZIKV), repetitive and finally non-repetitive (GRCh38) genomes. Bowtie2 indexes
570 were generated using the 'bowtie2-build' command in Bowtie2 for the ZIKV (KU501215.1)
571 RNA genome sequences. The specific parameters used for the FAST-iCLIP pipeline were
572 as follows: -f 18 (trims 17 nt from the 5′ end of the read), -l 16 (includes all reads longer
573 than 16 nt), –bm 29 (minimum MAPQ score from bowtie2 of 29 is required for mapping;
574 unique mapping only), –tr 2,3 (repetitive genome) and –tn 2,3 (non-repetitive genome)
575 RT stop intersection (n,m; where n = replicate number and m = number of unique RT
576 stops required per n replicates). Using the –tr/tn 2,3 parameters, a minimum of six RT
577 stops are required to support any single nucleotide identified as a crosslinking site.

578

579 Analysis of the sequencing data was performed using a custom analysis pipeline, with
580 the peak finding software uploaded to Github (https://github.com/ChangLab/FAST-
581 iCLIP/tree/lite). Other analyses were performed by aligning the reads to the human
582 genome using STAR, followed by gene counts using Bedtools (AR & IM, 2010). Only
583 reads in the canonical 3'UTR of the human transcripts were counted. The count
584 distribution across the metagene of the CDS and 3'UTRs was visualized using deeptools
585 (F, F, S, BA, & T, 2014). Log_2 fold changes were calculated by comparing RPKM values
586 between Mock and ZIKV infected cells. Genes with less than 10 total read counts were
587 excluded from analysis.

588

589 Heat maps and XY plots were produced using Prism 8 (GraphPad).

590

591 For total RNA and cytoplasmic/nuclear fractionated sequencing, reads were aligned to
592 the human genome using the STAR aligner (A et al., 2013) (version 2.7.5) followed by
593 HTSeq (S, PT, & W, 2015) (version 0.12.3) to obtain counts and then using the DeSeq2
594 (MI, W, & S, 2014) (version 1.28.1) pipeline to determine log_2 fold changes in transcripts.
595 Volcano plots were produced using the R-package, Enhanced Volcano
596 (https://github.com/kevinblighe/EnhancedVolcano).

597

598 **Acknowledgements**

599 Library preparation and QCs for sequencing was conducted by Mylinh Bernardi at the
600 Gladstone Genomics Core. The James B. Pendleton Charitable Trust supported the

601 sequencing on the NextSeq 500. Meredith Calvert and Blaise Ndjamen of the Gladstone
602 Histology and Light Microscopy core assisted with imaging and image analysis. Reuben
603 Thomas in the Gladstone Bioinformatics core provided statistical analysis help. Wendy
604 Runyon in the Gladstone Stem Cell core helped with iPSC maintenance. John Caroll
605 provided graphic design expertise, and Kathryn Claiborn provided manuscript editing.
606
607 **Funding**
608 This work was supported by the UCSF Medical Scientist Training Program (KEL), the
609 UCSF Biomedical Sciences Program (KEL), the NINDS/NIH under award F31NS113432
610 (KEL), the NIAID/NIH under award 5R01AI097552-03 (KEL, MO), NIDA/NIH under award
611 5DP1DA038043-05 (KEL, MO), NIH/NIAID F32AI112262 (PSS), NIH/NINDS R01
612 NS101996-01 (SF), NIH/NIAID U19AI1186101 to (NJK), DOD/DARPA HR0011-11-C-
613 0094 (PROPHECY, NJK), the Ottellini Family Discovery Fellowship (KEL), Damon
614 Runyon Cancer Research Foundation DRG-2286-17 (R.A.F.), and the James B.
615 Pendleton Charitable Trust.
616
617 **Author Contributions**
618 KEL, MO contributed to experimental design, data acquisition, data analysis and
619 manuscript writing. RAF, CB, JEC contributed to experimental design, data acquisition
620 and data analysis. MK, CS contributed to data acquisition. KAF, TN, ST and GRK
621 contributed to experimental design and data analysis. DJ-M, PSS and NJK contributed
622 with computational analysis. MD, JK and SF contributed assistance with data acquisition.
623

Competing Interests

No competing or conflicts of interest to report.

647

648

649

650

651

652

653

654

655 **Supplemental Figures**

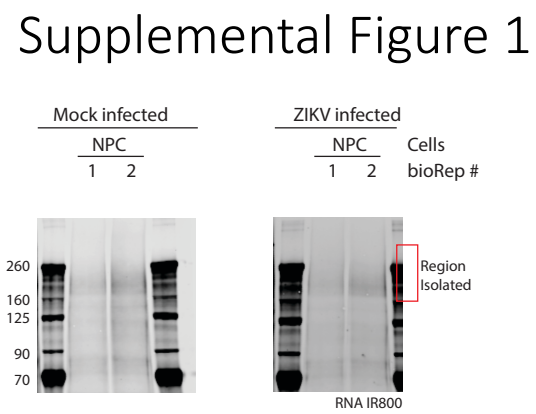

656

657 Supplemental Figure 1: Electrophoresis of RNA pulled down with UPF1, visualized using

658 the IR handle ligated to the RNAs. The region bounded by the red box indicates the part

659 of the gel excised and then analyzed by irCLIP and AP-MS. AP-MS analysis is indicated

660 in Supplemental File 1.

Supplemental Figure 2

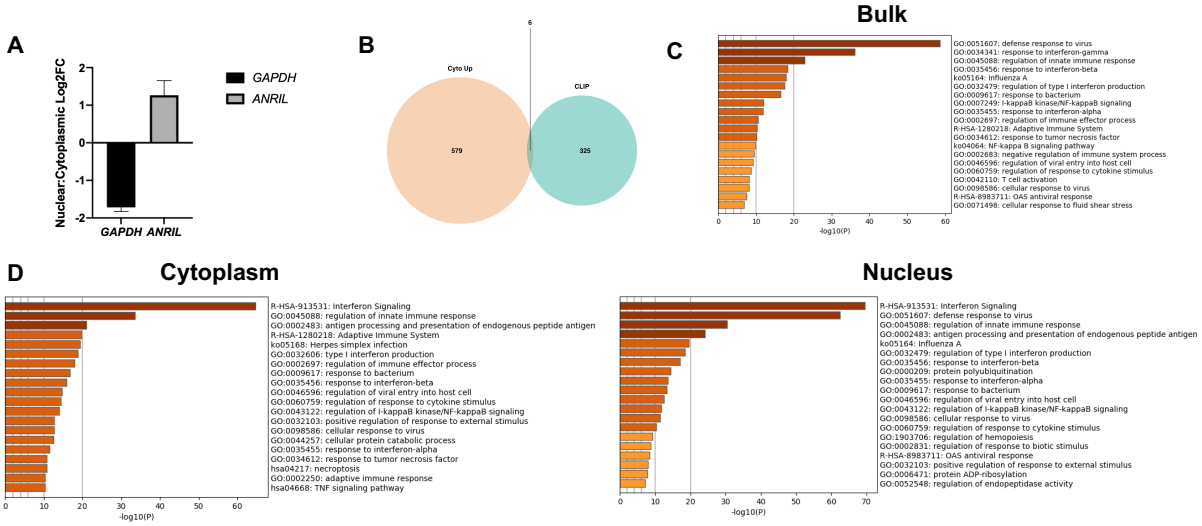

Supplemental Figure 2

A) Log_2 fold change from the fractionated RNA-sequencing between the nucleus and cytoplasm for markers of successful fractionation in the mock infected samples: GAPDH for cytoplasm and ANRIL for nucleus.

B) Comparison of transcripts increased in the cytoplasm and transcripts that lost interaction with UPF1 as determined by CLIP. Only 6 transcripts overlapped between the two groups.

C) Metascape Analysis of significantly upregulated transcripts found in the bulk RNA sequencing of Figure 2A. The top 400 upregulated genes were used to produce this GO clustering.

673 D) Metascape Analysis of significantly upregulated transcripts found in the
674 cytoplasmic and nuclear fractionated RNA sequencing of Figure 2D. The top 400
675 and 300 upregulated genes were used to produce this GO clustering.

Supplemental Figure 3

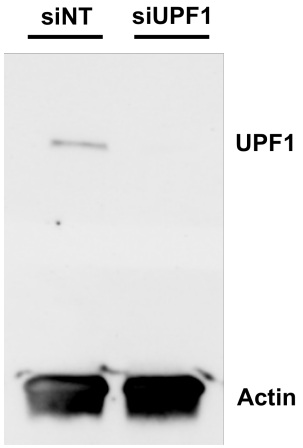

676

677 Supplemental Figure 3

678 Western blot for UPF1 in siNT and siUPF1 treated cells. Actin is shown as a loading
679 control.

680

Supplemental Figure 4

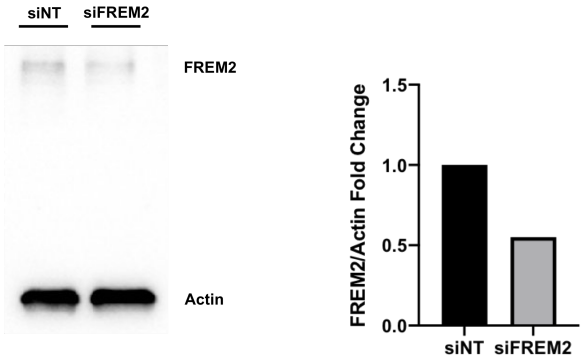

Supplemental Figure 4:

Western blot for FREM2 in siNT and siFREM2 treated NPCs after 7 days. Densitometric analyses of FREM2 were performed using ImageJ to quantify relative band intensities

References

A, D., CA, D., F, S., J, D., C, Z., S, J., . . . TR, G. (2013). STAR: ultrafast universal RNA-seq aligner. *Bioinformatics (Oxford, England), 29*(1). doi:10.1093/bioinformatics/bts635

Ajamian, L., Abel, K., Rao, S., Vyboh, K., Garcia-de-Gracia, F., Soto-Rifo, R., . . . Mouland, A. J. (2015). HIV-1 Recruits UPF1 but Excludes UPF2 to Promote Nucleocytoplasmic Export of the Genomic RNA. *Biomolecules, 5*(4), 2808-2839. doi:10.3390/biom5042808

AR, Q., & IM, H. (2010). BEDTools: a flexible suite of utilities for comparing genomic features. *Bioinformatics (Oxford, England), 26*(6). doi:10.1093/bioinformatics/btq033

Balistreri, G., Bognanni, C., & Mühlemann, O. (2017). Virus Escape and Manipulation of Cellular Nonsense-Mediated mRNA Decay. *Viruses, 9*(1). doi:10.3390/v9010024

BJ, Z., RA, F., Y, S., BT, D., HY, C., & PA, K. (2016). irCLIP platform for efficient characterization of protein-RNA interactions. *Nature Methods, 13*(6). doi:10.1038/nmeth.3840

Carmody, S. R., & Wente, S. R. (2009). mRNA nuclear export at a glance. *J Cell Sci, 122*(Pt 12), 1933-1937. doi:10.1242/jcs.041236

Chawla, R., Redon, S., Raftopoulou, C., Wischnewski, H., Gagos, S., & Azzalin, C. M. (2011). Human UPF1 interacts with TPP1 and telomerase and sustains telomere leading-strand replication. *The EMBO Journal, 30*(19), 4047-4058. doi:10.1038/emboj.2011.280

718 Consortium, H. i. (2017). Developmental alterations in Huntington's disease neural cells
719 and pharmacological rescue in cells and mice. *Nat Neurosci, 20*(5), 648-660.
720 doi:10.1038/nn.4532
721 Costa, F., Sarno, M., Khouri, R., de Paula Freitas, B., Siqueira, I., Ribeiro, G. S., . . .
722 Almeida, A. R. (2016). Emergence of Congenital Zika Syndrome: Viewpoint From
723 the Front Lines. *Ann Intern Med, 164*(10), 689-691. doi:10.7326/m16-0332
724 Cugola, F. R., Fernandes, I. R., Russo, F. B., Freitas, B. C., Dias, J. L. M., Guimarães,
725 K. P., . . . Beltrão-Braga, P. C. B. (2016). The Brazilian Zika virus strain causes
726 birth defects in experimental models. *Nature, 534*(7606), 267-271.
727 doi:10.1038/nature18296
728 de Paula Freitas, B., Ventura, C. V., Maia, M., & Belfort, R., Jr. (2017). Zika virus and
729 the eye. *Curr Opin Ophthalmol, 28*(6), 595-599.
730 doi:10.1097/icu.0000000000000420
731 F, R., F, D., S, D., BA, G., & T, M. (2014). deepTools: a flexible platform for exploring
732 deep-sequencing data. *Nucleic Acids Research, 42*(Web Server issue).
733 doi:10.1093/nar/gku365
734 Fauci, A. S., & Morens, D. M. (2016). Zika Virus in the Americas--Yet Another Arbovirus
735 Threat. *The New England Journal of Medicine, 374*(7), 601-604.
736 doi:10.1056/NEJMp1600297
737 Feng, Q., Jagannathan, S., & Bradley, R. K. (2017). The RNA Surveillance Factor UPF1
738 Represses Myogenesis via Its E3 Ubiquitin Ligase Activity. *Molecular Cell, 67*(2),
739 23-251.e256. doi:10.1016/j.molcel.2017.05.034

740 Fiorini, F., Bagchi, D., Le Hir, H., & Croquette, V. (2015). Human Upf1 is a highly
741 processive RNA helicase and translocase with RNP remodelling activities. *Nat*
742 *Commun, 6*, 7581. doi:10.1038/ncomms8581
743 Fontaine, K. A., Leon, K. E., Khalid, M. M., Tomar, S., Jimenez-Morales, D., Dunlap, M.,
744 . . . Ott, M. (2018). The Cellular NMD Pathway Restricts Zika Virus Infection and
745 Is Targeted by the Viral Capsid Protein. *mBio, 9*(6). doi:10.1128/mBio.02126-18
746 Fortes, P., Beloso, A., & Ortín, J. (1994). Influenza virus NS1 protein inhibits pre-mRNA
747 splicing and blocks mRNA nucleocytoplasmic transport. *Embo j, 13*(3), 704-712.
748 Gehring, N. H., Lamprinaki, S., Kulozik, A. E., & Hentze, M. W. (2009). Disassembly of
749 exon junction complexes by PYM. *Cell, 137*(3), 536-548.
750 doi:10.1016/j.cell.2009.02.042
751 Gehring, N. H., Neu-Yilik, G., Schell, T., Hentze, M. W., & Kulozik, A. E. (2003). Y14
752 and hUpf3b Form an NMD-Activating Complex. *Molecular Cell, 11*(4), 939-949.
753 doi:https://doi.org/10.1016/S1097-2765(03)00142-4
754 Göertz, G. P., Abbo, S. R., Fros, J. J., & Pijlman, G. P. (2018). Functional RNA during
755 Zika virus infection. *Virus Res, 254*, 41-53. doi:10.1016/j.virusres.2017.08.015
756 Imamachi, N., Salam, K. A., Suzuki, Y., & Akimitsu, N. (2017). A GC-rich sequence
757 feature in the 3′ UTR directs UPF1-dependent mRNA decay in mammalian cells.
758 *Genome Res, 27*(3), 407-418. doi:10.1101/gr.206060.116
759 Kebaara, B. W., & Atkin, A. L. (2009). Long 3′-UTRs target wild-type mRNAs for
760 nonsense-mediated mRNA decay in Saccharomyces cerevisiae. In *Nucleic Acids*
761 *Res* (Vol. 37, pp. 2771-2778).

762 Kim, Y. K., & Maquat, L. E. (2019). UPFront and center in RNA decay: UPF1 in
763 nonsense-mediated mRNA decay and beyond. *RNA, 25*(4), 407-422.
764 doi:10.1261/rna.070136.118
765 Kumar, G. R., & Glaunsinger, B. A. (2010). Nuclear import of cytoplasmic poly(A)
766 binding protein restricts gene expression via hyperadenylation and nuclear
767 retention of mRNA. *Mol Cell Biol, 30*(21), 4996-5008. doi:10.1128/mcb.00600-10
768 Kurosaki, T., & Maquat, L. E. (2016). Nonsense-mediated mRNA decay in humans at a
769 glance. *J Cell Sci, 129*(3), 461-467. doi:10.1242/jcs.181008
770 Kurosaki, T., Popp, M. W., & Maquat, L. E. (2019). Quality and quantity control of gene
771 expression by nonsense-mediated mRNA decay. *Nat Rev Mol Cell Biol, 20*(7),
772 406-420. doi:10.1038/s41580-019-0126-2
773 Kuss, S. K., Mata, M. A., Zhang, L., & Fontoura, B. M. (2013). Nuclear imprisonment:
774 viral strategies to arrest host mRNA nuclear export. *Viruses, 5*(7), 1824-1849.
775 doi:10.3390/v5071824
776 Leon, K., & Ott, M. (2020). An 'Arms Race' between the Nonsense-mediated mRNA
777 Decay Pathway and Viral Infections. *Seminars in cell & developmental biology*.
778 doi:10.1016/j.semcdb.2020.05.018
779 Li, C., Xu, D., Xu, Z., Ye, Q., Hong, S., Jiang, Y., . . . Qin, C.-F. (2016). Zika Virus
780 Disrupts Neural Progenitor Development and Leads to Microcephaly in Mice. *Cell*
781 *Stem Cell, 19*(1), 120-126. doi:10.1016/j.stem.2016.04.017
782 Li, M., Johnson, J. R., Truong, B., Kim, G., Weinbren, N., Dittmar, M., . . . Ramage, H.
783 (2019). Identification of antiviral roles for the exon-junction complex and

784 nonsense-mediated decay in flaviviral infection. *Nat Microbiol, 4*(6), 985-995.
785 doi:10.1038/s41564-019-0375-z
786 Liu, L., Chen, Z., Zhang, X., Li, S., Hui, Y., Feng, H., . . . Zhang, X. (2019). Protection of
787 ZIKV infection-induced neuropathy by abrogation of acute antiviral response in
788 human neural progenitors. *Cell Death Differ, 26*(12), 2607-2621.
789 doi:10.1038/s41418-019-0324-7
790 Loh, B., Jonas, S., & Izaurralde, E. (2013). The SMG5-SMG7 heterodimer directly
791 recruits the CCR4-NOT deadenylase complex to mRNAs containing nonsense
792 codons via interaction with POP2. *Genes Dev, 27*(19), 2125-2138.
793 doi:10.1101/gad.226951.113
794 Lykke-Andersen, S., Chen, Y., Ardal, B. R., Lilje, B., Waage, J., Sandelin, A., & Jensen,
795 T. H. (2014). Human nonsense-mediated RNA decay initiates widely by
796 endonucleolysis and targets snoRNA host genes. *Genes Dev, 28*(22), 2498-
797 2517. doi:10.1101/gad.246538.114
798 Martínez-Cerdeño, V., & Noctor, S. C. (2018). Neural Progenitor Cell Terminology.
799 *Front Neuroanat, 12*, 104. doi:10.3389/fnana.2018.00104
800 MI, L., W, H., & S, A. (2014). Moderated estimation of fold change and dispersion for
801 RNA-seq data with DESeq2. *Genome biology, 15*(12). doi:10.1186/s13059-014-
802 0550-8
803 Mohd Ropidi, M. I., Khazali, A. S., Nor Rashid, N., & Yusof, R. (2020). Endoplasmic
804 reticulum: a focal point of Zika virus infection. *J Biomed Sci, 27*(1), 27.
805 doi:10.1186/s12929-020-0618-6

806 Musso, D., & Gubler, D. J. (2016). Zika Virus. *Clinical Microbiology Reviews, 29*(3), 487-
807 524. doi:10.1128/cmr.00072-15
808 Ojha, C. R., Rodriguez, M., Lapierre, J., Muthu Karuppan, M. K., Branscome, H.,
809 Kashanchi, F., & El-Hage, N. (2018). Complementary Mechanisms Potentially
810 Involved in the Pathology of Zika Virus. *Frontiers in immunology, 9*, 2340-2340.
811 doi:10.3389/fimmu.2018.02340
812 Oliveira, E. R. A., Mohana-Borges, R., de Alencastro, R. B., & Horta, B. A. C. (2017).
813 The flavivirus capsid protein: Structure, function and perspectives towards drug
814 design. *Virus Res, 227*, 115-123. doi:10.1016/j.virusres.2016.10.005
815 Pavlakis, E., Chiotaki, R., & Chalepakis, G. (2011). The role of Fras1/Frem proteins in
816 the structure and function of basement membrane. *Int J Biochem Cell Biol, 43*(4),
817 487-495. doi:10.1016/j.biocel.2010.12.016
818 Peccarelli, M., & Kebaara, B. W. (2014). Regulation of natural mRNAs by the nonsense-
819 mediated mRNA decay pathway. *Eukaryot Cell, 13*(9), 1126-1135.
820 doi:10.1128/ec.00090-14
821 Pierson, T. C., & Diamond, M. S. (2018). The emergence of Zika virus and its new
822 clinical syndromes. *Nature, 560*(7720), 573-581. doi:10.1038/s41586-018-0446-y
823 Popp, M. W., & Maquat, L. E. (2013). Organizing principles of mammalian nonsense-
824 mediated mRNA decay. *Annu Rev Genet, 47*, 139-165. doi:10.1146/annurev-
825 genet-111212-133424
826 Roth, H., Magg, V., Uch, F., Mutz, P., Klein, P., Haneke, K., . . . Ruggieri, A. (2017).
827 Flavivirus Infection Uncouples Translation Suppression from Cellular Stress
828 Responses. *mBio, 8*(1). doi:10.1128/mBio.02150-16

829 S, A., PT, P., & W, H. (2015). HTSeq--a Python framework to work with high-throughput
830 sequencing data. *Bioinformatics (Oxford, England), 31*(2).
831 doi:10.1093/bioinformatics/btu638
832 Sakuma, T., Davila, J. I., Malcolm, J. A., Kocher, J. P., Tonne, J. M., & Ikeda, Y. (2014).
833 Murine leukemia virus uses NXF1 for nuclear export of spliced and unspliced
834 viral transcripts. *J Virol, 88*(8), 4069-4082. doi:10.1128/jvi.03584-13
835 Schneider, C. A., Rasband, W. S., & Eliceiri, K. W. (2012). NIH Image to ImageJ: 25
836 years of image analysis. *Nature Methods, 9*(7), 671-675.
837 doi:10.1038/nmeth.2089
838 Shao, Q., Herrlinger, S., Yang, S.-L., Lai, F., Moore, J. M., Brindley, M. A., & Chen, J.-F.
839 (2016). Zika virus infection disrupts neurovascular development and results in
840 postnatal microcephaly with brain damage. *Development (Cambridge, England),*
841 *143*(22), 4127-4136. doi:10.1242/dev.143768
842 Singh, A. K., Choudhury, S. R., De, S., Zhang, J., Kissane, S., Dwivedi, V., . . . Brogna,
843 S. (2019). The RNA helicase UPF1 associates with mRNAs co-transcriptionally
844 and is required for the release of mRNAs from gene loci. *eLife, 8*.
845 doi:10.7554/eLife.41444
846 Slavotinek, A. M., & Tifft, C. J. (2002). Fraser syndrome and cryptophthalmos: review of
847 the diagnostic criteria and evidence for phenotypic modules in complex
848 malformation syndromes. *J Med Genet, 39*(9), 623-633.
849 doi:10.1136/jmg.39.9.623
850 Souza, B. S. F., Sampaio, G. L. A., Pereira, C. S., Campos, G. S., Sardi, S. I., Freitas,
851 L. A. R., . . . Soares, M. B. P. (2016). Zika virus infection induces mitosis

852 abnormalities and apoptotic cell death of human neural progenitor cells. *Scientific*
853 *reports, 6*(1), 39775. doi:10.1038/srep39775
854 Stoeckli, E. T. (2018). Understanding axon guidance: are we nearly there yet?
855 *Development, 145*(10). doi:10.1242/dev.151415
856 Tang, H., Hammack, C., Ogden, Sarah C., Wen, Z., Qian, X., Li, Y., . . . Ming, G.-l.
857 (2016). Zika Virus Infects Human Cortical Neural Progenitors and Attenuates
858 Their Growth. *Cell Stem Cell, 18*(5), 587-590. doi:10.1016/j.stem.2016.02.016
859 Timmer, J. R., Mak, T. W., Manova, K., Anderson, K. V., & Niswander, L. (2005). Tissue
860 morphogenesis and vascular stability require the Frem2 protein, product of the
861 mouse myelencephalic blebs gene. *Proc Natl Acad Sci U S A, 102*(33), 11746-
862 11750. doi:10.1073/pnas.0505404102
863 Toma, K. G., Rebbapragada, I., Durand, S., & Lykke-Andersen, J. (2015). Identification
864 of elements in human long 3' UTRs that inhibit nonsense-mediated decay. *RNA,*
865 *21*(5), 887-897. doi:10.1261/rna.048637.114
866 Varsally, W., & Brogna, S. (2012). UPF1 involvement in nuclear functions. *Biochem Soc*
867 *Trans, 40*(4), 778-783. doi:10.1042/bst20120052
868 Ventura, C. V., & Ventura, L. O. (2018). Ophthalmologic Manifestations Associated With
869 Zika Virus Infection. *Pediatrics, 141*(Suppl 2), S161-s166.
870 doi:10.1542/peds.2017-2038E
871 Vicenti, I., Boccuto, A., Giannini, A., Dragoni, F., Saladini, F., & Zazzi, M. (2018).
872 Comparative analysis of different cell systems for Zika virus (ZIKV) propagation
873 and evaluation of anti-ZIKV compounds in vitro. *Virus Res, 244*, 64-70.
874 doi:10.1016/j.virusres.2017.11.003

875 Zarnegar, B. J., Flynn, R. A., Shen, Y., Do, B. T., Chang, H. Y., & Khavari, P. A. (2016).
876 irCLIP platform for efficient characterization of protein-RNA interactions. *Nat*
877 *Methods, 13*(6), 489-492. doi:10.1038/nmeth.3840
878